



## RESEARCH ARTICLE

10.1002/2017JE005282

## Key Points:

- In places, the smooth plains inside and outside the Caloris Basin are contiguous
- They were emplaced during the same time period
- Spectral and compositional differences reflect local source composition and imply 100 km, rather than 1000 km, flow lengths

## Correspondence to:

D. A. Rothery,  
d.a.rothery@open.ac.uk

## Citation:

Rothery, D. A., P. Mancinelli, L. Guzzetta, and J. Wright (2017), Mercury's Caloris basin: Continuity between the interior and exterior plains, *J. Geophys. Res. Planets*, 122, 560–576, doi:10.1002/2017JE005282.

Received 8 FEB 2017

Accepted 23 FEB 2017

Accepted article online 6 MAR 2017

Published online 20 MAR 2017

## Mercury's Caloris basin: Continuity between the interior and exterior plains

David A. Rothery<sup>1</sup>, Paolo Mancinelli<sup>2</sup> , Laura Guzzetta<sup>3</sup> , and Jack Wright<sup>1</sup>

<sup>1</sup>School of Physical Sciences, Open University, Milton Keynes, UK, <sup>2</sup>Dipartimento di Fisica e Geologia, Università degli Studi di Perugia, Perugia, Italy, <sup>3</sup>Istituto di Astrofisica e Planetologia Spaziali, INAF, Rome, Italy

**Abstract** The smooth plains on the floor of Mercury's Caloris basin and those almost entirely surrounding it beyond its rim are usually accepted to be younger than the rim materials and to be lava flows rather than impact melt. High-resolution imaging shows that the emplacement of interior and exterior plains was concurrent, with evidence of both inward and outward flow while they were being emplaced. The Caloris rim is breached in two places by continuous smooth plains that seamlessly connect interior and exterior plains. The gross-scale spectral and compositional distinctiveness of interior and exterior plains is blurred on a scale of several tens of kilometers, which could reflect interfingering of flow units less than a few hundred kilometers long that tapped melt sources of different composition and/or depth inside and outside the basin followed by local mixing of regolith. Flows occurring both inside and outside the basin should be included in estimates of the total erupted volume.

**Plain Language Summary** The “smooth plains” interpreted to be lava flows inside and outside Mercury's Caloris basin have different color and different composition when viewed on broad scale. However, study of the highest-resolution images from NASA's MExcury Surface, Space ENvironment, GEochemistry, and Ranging (MESSENGER) mission reveals places where there is a continuous lava surface between the interior and exterior plains and a gradual, not sharp, color change. There are also places where exterior plains lava has cascaded over the basin rim toward the basin floor and others where the interior plains seem to flood outward against or over the rim. It seems that interior and exterior plains were made by flood volcanism occurring during an overlapping time period. The lack of a sharp color boundary between the interior and exterior plains is evidence of multiple individual flow units that were less than a few hundred kilometers in length.

### 1. Introduction

Mercury's largest well-preserved impact basin is 1550 km in diameter (Figure 1). It has no formal name but is usually referred to as “the Caloris basin,” taking this appellation from Caloris Planitia, which is the International Astronomical Union-approved name of the “smooth plains” that cover the basin floor, and the eastern part of its rim that is mapped as Caloris Montes. On a gross scale, the plains are spectrally [Denevi *et al.*, 2009; Izenberg *et al.*, 2014; Ernst *et al.*, 2015; Murchie *et al.*, 2008, 2015] and compositionally [Weider *et al.*, 2015] distinct from the plains outside the basin, though the effective spatial resolution of even the best X-ray spectroscopy [Weider *et al.*, 2015] in this region is of the order of 100 km.

For clarity in what follows, we refer to the plains units inside and surrounding the basin as “interior plains” and “exterior plains,” respectively, while recognizing that both can be legitimately described and mapped as smooth plains. In agreement with most other authors of the MExcury Surface, Space ENvironment, GEochemistry, and Ranging (MESSENGER) era, we accept that these were emplaced largely by effusive volcanism prior to about 3.5 Ga [Head *et al.*, 2009; Denevi *et al.*, 2013; Ernst *et al.*, 2015; Murchie *et al.*, 2015; Byrne *et al.*, 2016]. The vents or fissures through which these were erupted are not identifiable.

Based on the density of superposed craters, most simply  $N(10)$  and  $N(20)$  values (the number of craters whose diameters exceed 10 and 20 km per million square kilometers), Caloris rim terrain is resolvably older than the interior and exterior plains [Fassett *et al.*, 2009], both of which embay the rim. We accept this as evidence that neither of these plains units can be impact melt nor ejecta from the basin-forming event.

The use of crater counting to determine the relative ages of the interior and exterior plains has proven intractable, despite claims that the exterior plains are slightly the younger of the two [Murray *et al.*, 1975; Strom *et al.*, 2008; Fassett *et al.*, 2009]. This is because the standard errors on the counts overlap,

©2017. The Authors.

This is an open access article under the terms of the Creative Commons Attribution License, which permits use, distribution and reproduction in any medium, provided the original work is properly cited.

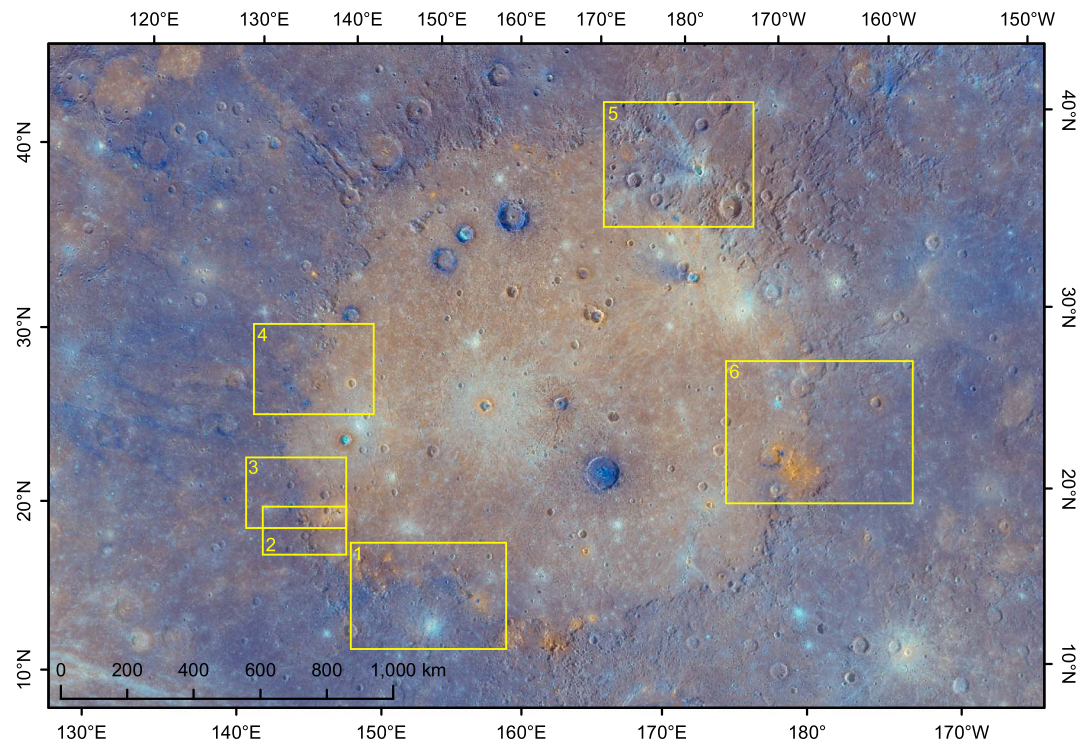


**Figure 1.** Enhanced color view [Robinson *et al.*, 2008; Denevi *et al.*, 2009] of the Caloris basin, in which the interior plains are red and belong to a spectrally defined subset of smooth plains called “high-reflectance red plains” that occurs also in Mercury’s northern plains, beyond the region shown here. The exterior plains belong to a spectrally defined subset of smooth plains called “low-reflectance blue plains”; at this scale they are hard to distinguish from rougher and more elevated terrain around the basin rim constituting units of the Caloris Group [McCauley *et al.*, 1981]. Numbers 1–6 identify locations studied in this paper.

whether expressed as  $N(10)$  and  $N(20)$  [Fassett *et al.*, 2009; Denevi *et al.*, 2013] or as model ages [Mancinelli *et al.*, 2016]. Apart from the usual uncertainties regarding the exclusion of secondary craters from the count, relative dating of surfaces of similar age is further compromised because of possible differences in target properties such as density, strength, and thickness [e.g., Holsapple and Housen, 2007], in this region likely present due to flow thickness, buried impact melt thickness, and basement fracturing, which could all differ between the interior and exterior of the basin.

Here we adopt an alternative approach toward determining the relationship between interior and exterior plains, by looking for volcanological and morphological evidence in the highest-resolution images returned by MESSENGER [Chabot *et al.*, 2016], which orbited Mercury 2011–2015 [McNutt *et al.*, 2014; Rothery, 2015]. These are Mercury Dual Imaging System (MDIS) narrow-angle camera (NAC) images [Hawkins *et al.*, 2007]. We examined MDIS panchromatic global mosaics at 250 and 166 mpp (meters per pixel) supplemented by an enhanced color (see section 5) wide-angle camera (WAC) mosaic at 665 mpp and a standard three-band color mosaic at 333 mpp, to identify the critical locations where the Caloris rim is breached such that interior and exterior plains are in contact. We then searched for and selected the highest-resolution NAC images within each critical location, typically ranging from 14 mpp to 110 mpp. We then interpreted these from a primarily volcanological perspective. In doing so, we set aside any constraint to distinguish flow units that are conventionally mapped as likely impact melt, to see if we could construct a volcanological story consistent with the crater counting that indicates that the flow units are younger than the rim [Fassett *et al.*, 2009].

We examined topography according to a 665 mpp global digital elevation model derived by stereo imaging [Becker *et al.*, 2016] (Figure 2), mindful that the long-wavelength topographic undulations [Oberst *et al.*, 2010; Zuber *et al.*, 2012; Byrne *et al.*, 2014] (and possibly also more local effects) make the directions of regional and some low-gradient local slopes untrustworthy as a guide to the situation during flow emplacement. Undulations trending east-west across Caloris can be seen in Figure 2.

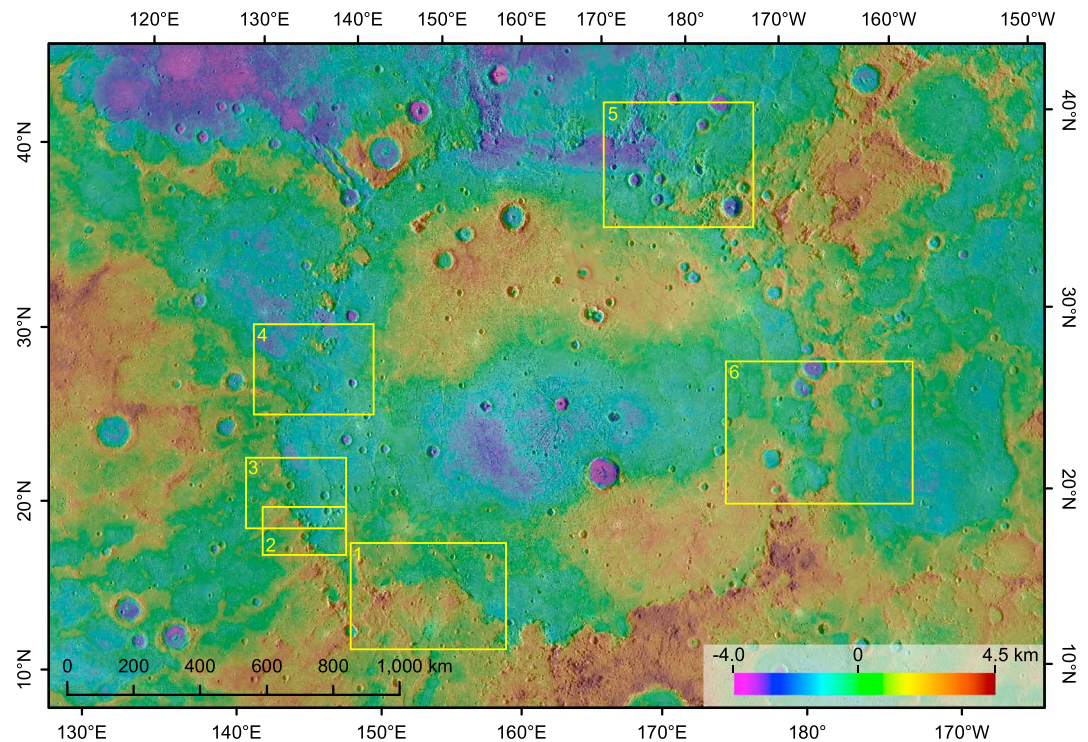


**Figure 2.** Color-coded topography of the Caloris basin.

Topography and gravity admittance analysis [James *et al.*, 2015] shows thinner than usual crust and anomalously low-density mantle in the Caloris basin and hence likely different melting conditions for locally sourced smooth plains compared with sources beyond the basin. The lack of embayed or ghost craters on the interior plains is regarded [Ernst *et al.*, 2015] as most likely to demonstrate either at least 2.5 km of lava burying any craters that formed on the basin floor prior to basin fill lava emplacement or else insufficient time for large craters to have formed before this occurred.

## 2. Background to the Caloris Rim

The inward facing scarp marking the edge of the Caloris basin is up to 3 km above the level of the interior plains, notably along much of the southern rim. Elsewhere, it is lower, and in a few places it lacks clear topographic expression. There, the place where scarp would be expected has become flooded by smooth plains, and it is unclear whether this is because there was an original gap in the rim or just a relatively low point in the rim. Where best exposed (least flooded by smooth plains), the scarp has a distinctive morphology, usually consisting of straight-sided reentrants from less than 10 km to nearly 100 km in size (e.g., 179.4°W 38.4°N and 177.3°E 17.3°N). Some regions of interior plains within 150 km of the rim surround and embay isolated flat-topped blocks of probable rim material up to 40 km in size (e.g., 149.8°E, 42.7°N). These aspects are similar to some lunar basin rims, notably part of the SE rim of the Imbrium basin and parts of Montes Rook in the Orientale basin (both noted by Fassett *et al.* [2009]) and much of the rim of Mare Crisium. Also mirrored on the Moon (for example, between parts of the Montes Rook and Montes Cordillera surrounding Orientale and beyond the northern rim of Imbrium [Denevi *et al.*, 2013, Figure 11]) is terrain beyond the Caloris rim marked by numerous isolated knobs of Caloris ejecta embayed (and on some interpretations mantled) by smooth plains that could be either volcanic or impact melt [Fassett *et al.*, 2009]. This is the Odin Formation of McCauley *et al.* [1981]. This unit does not lend itself to consistent mapping, because the lower size limit of knobs to include and the minimum spacing between blocks to exclude are affected by both personal preference and mapping scale. For example, on the west side of Caloris, some workers [Goosmann *et al.*, 2016] show extensive Odin Formation, whereas others [Mancinelli *et al.*, 2016] show much of this as (exterior) smooth plains and subdivide the remainder with the addition of an extra unit that they term “Caloris Rough Ejecta.”

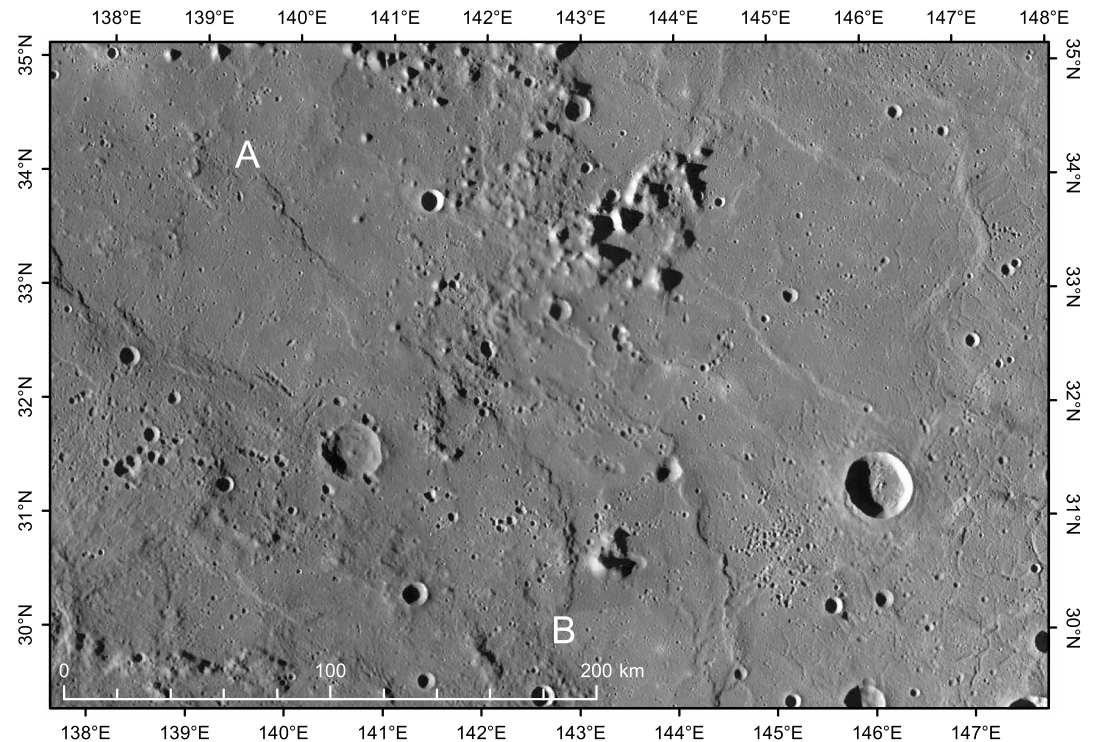


**Figure 3.** Location 4, 166 mpp NAC mosaic. Embayed blocks of rim material at 143–144°E are just within the rim of the basin, which runs north-south. A and B indicate ends of the wrinkle ridge of which the 80 km length extending north and west from B was chosen arbitrarily to mark the contact between exterior and interior plains in Mancinelli *et al.* [2016]. Point A is at least 100 km outside the basin. A possible flow front representing outward flow of interior plains can be traced from the northern edge of the frame at 142°E for 100 km southward, but it loses its identity before it reaches the A-B wrinkle ridge and could be a wrinkle ridge itself.

Several authors have remarked on the abundance of inferred pyroclastic deposits close inside the Caloris rim [Murchie *et al.*, 2008; Head *et al.*, 2011; Kerber *et al.*, 2009, 2011; Rothery *et al.*, 2014; Goudge *et al.*, 2014; Thomas *et al.*, 2014], based on the presence of vent-like features almost always surrounded by a diffuse-edged “red” area up to a few tens of kilometers across that was apparently dispersed from the vent by explosive eruptions. The inferred sources are always on smooth plains rather than on rim materials. Examples near the southern rim at 155–167°E are in scarp reentrants flooded by interior plains, and there is no example where the inferred source is definitely beyond the scarp. Furthermore, the candidate vents puncture the interior plains and their deposits are superimposed upon the plains, showing that this explosive phase of volcanism postdated the plains emplacement. We regard the candidate vents and pyroclastic deposits as incidental to the relationship between interior and exterior plains and do not discuss them further.

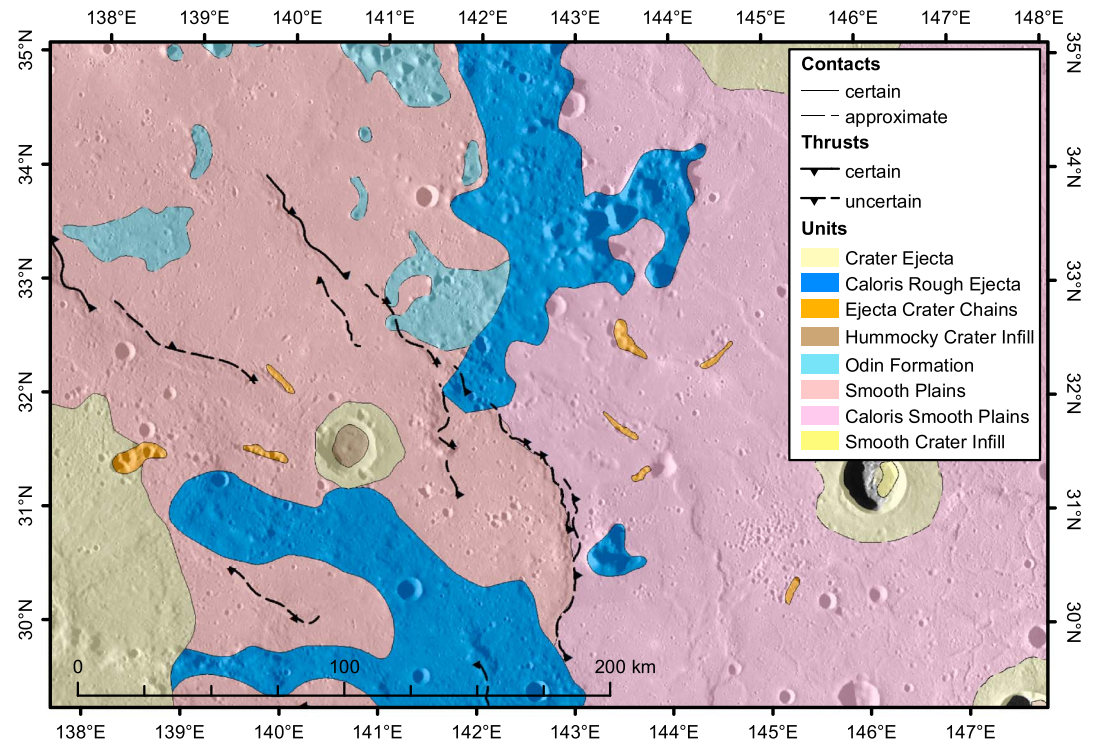
### 3. The Critical Locations

Figure 1 identifies locations where key relationships can be discerned between interior and exterior plains. We label these 1–6, starting in the south and working clockwise around the basin. Denevi *et al.* [2013] noted locations 1–3 as sites showing “evidence of flow from the lower-reflectance Odin-type deposits into the basin.” Here we study those and three more with the benefit of higher-resolution imaging and a wider variety of illumination conditions.

We first describe locations where the Caloris rim has been breached such that an apparently continuous plains unit extends between the interior and exterior of the basin. Next we examine locations where the rim remains apparent but the dominant evidence is of plains unit flow into the basin, and finally, we examine locations showing signs of outward flow.

#### 3.1. Plains Units Continuous Across the Caloris Rim

We present two examples: location 4 and 6 (see Figure 1 for location).



**Figure 4.** Location 4, exactly the same area as in Figure 3, showing the mapping of *Mancinelli et al.* [2016]. “Caloris smooth plains” correspond to our interior plains, and smooth plains correspond to our exterior plains. We regard the Odin Formation here merely as exterior plains embaying ejecta knobs. We have omitted symbols identifying wrinkle ridges and individual knobs in the Odin Formation.

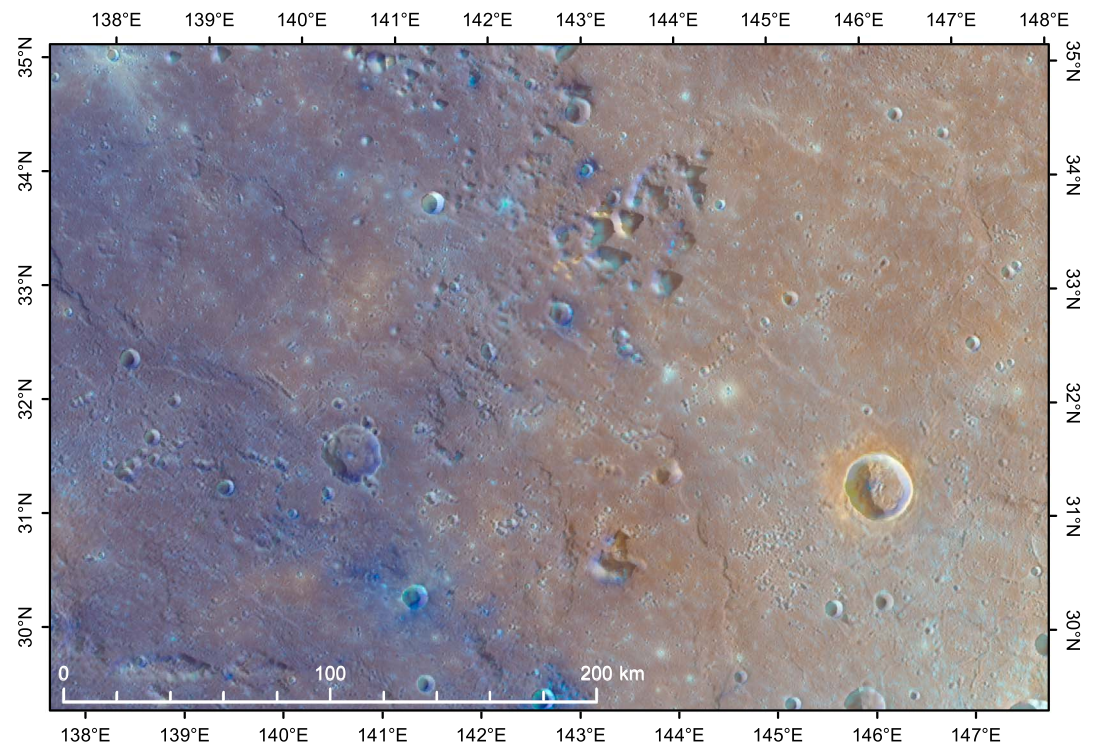


**Figure 5.** Location 4, with 665 mpp WAC color overlay on 166 mpp NAC mosaic. Note the diffuse and patchy gradual color transition between exterior plains (on the left) and interior plains (on the right).

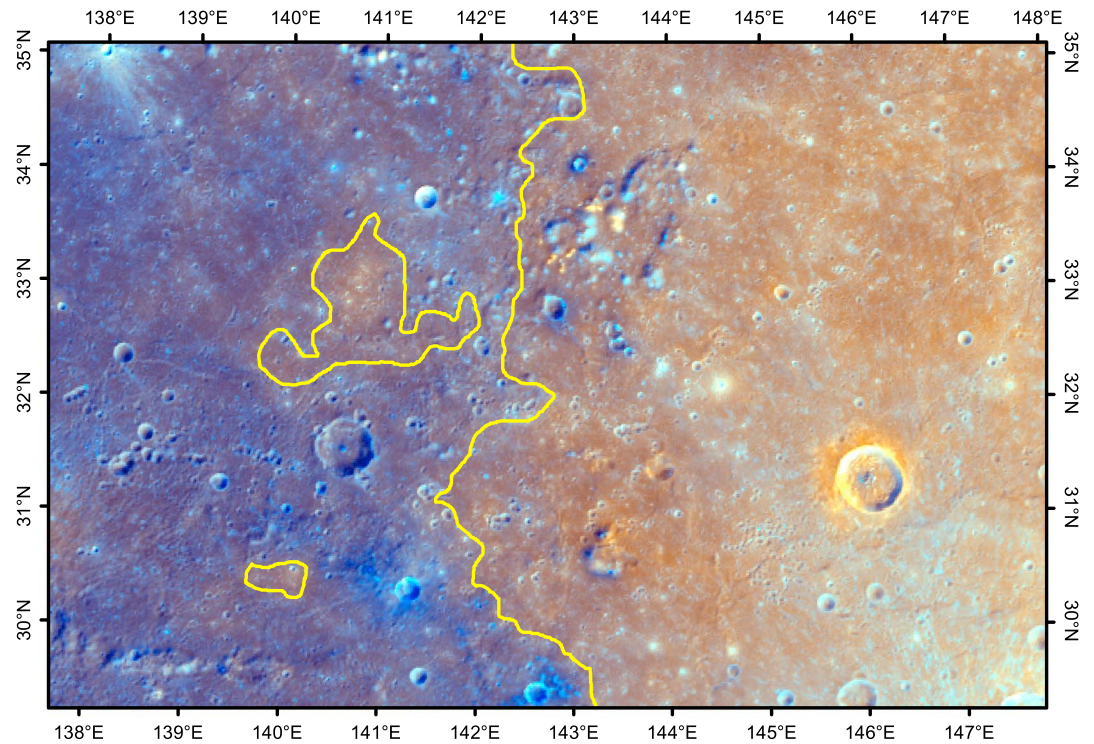


**Figure 6.** An example of simplified results of a supervised multispectral classification, superimposed on the color channels that were used in Figure 5. The yellow line near 143°E separates red interior plains from blue exterior plains. The two closed yellow lines outline red patches isolated within the blue unit. We show only those red patches larger than 100 km<sup>2</sup> and omit minor classes of other spectral type.

### 3.1.1. Location 4

In location 4, the basin rim was evidently so low (though probably not entirely lacking original surface expression) that smooth plains were able to overtop it completely, and the interior plains are in contact with undoubted exterior smooth plains [Goosmann *et al.*, 2016; Mancinelli *et al.*, 2016]. The total width of the breach is about 400 km, but here we focus on the central 200 km (Figure 3). This location falls within the 1:3 M quadrangle geologic map of Mancinelli *et al.* [2016], from which Figure 4 is an extract.

The “true” extent of the Odin Formation in Figure 4 is debatable, because the minimum number density of knobs necessary to classify an area as Odin Formation is undefined [McCauley *et al.*, 1981] and there is no robust reason to regard this terrain as anything other than ordinary smooth plains material that happens to have embayed some knobby terrain. We regard it as plausible that even in the areas mapped as Odin Formation the majority of flow material was volcanic lava rather than impact melt.

Faced with the requirement to distinguish interior and exterior plains, Mancinelli *et al.* [2016] placed the contact along a morphotectonic feature that they mapped as a “thrust-uncertain” (Figure 4). We can confirm that the study of the highest-resolution images of the “contact” (14 mpp) gives no reason to interpret this as anything other than an unremarkable wrinkle ridge. Local color changes (Figure 5) show no relationship with this feature. This is an area where it appears one could walk from exterior to interior plains without crossing an identifiable boundary. The transition from red interior plains to “blue” exterior plains is particularly diffuse and patchy in this region. This may be partly, though we think certainly not completely, because of streaks of blue ejecta from Raditladi, a 260 km diameter late Mansurian peak ring basin 1000 km to the west of the Caloris rim.

To confirm what was, to us, already visually apparent, we performed supervised maximum likelihood multispectral classification in Figure 5 and the surrounding region. We defined training areas on interior red plains, exterior blue plains, and (to avoid inappropriately forcing all pixels into one or other of the plains units) also bright crater ejecta and “low-reflectance material.” The example of our results shown in Figure 6 confirms that the Mancinelli *et al.* [2016] morphotectonic feature bears no relation to any spectral boundary and that the

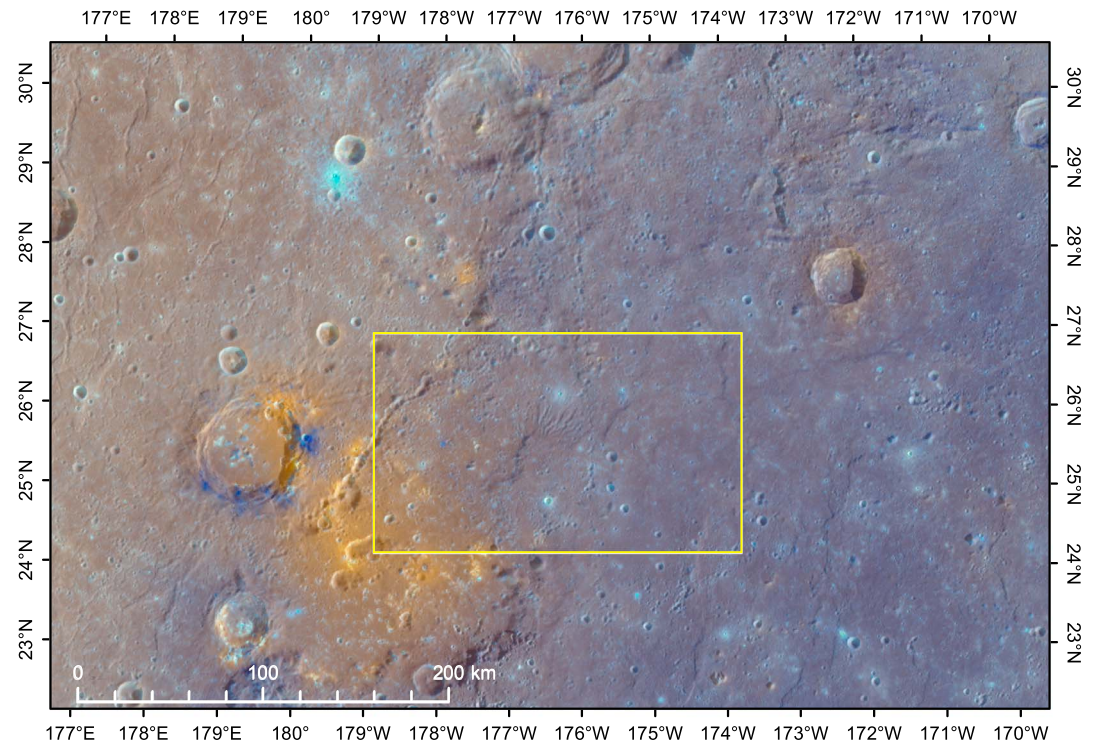


**Figure 7.** Location 6, with 665 mpp WAC color overlay on 166 mpp NAC mosaic. The largest crater cut by the top edge is March. High-reflectance reddish materials are associated with pyroclastic products erupted from local vents and are superimposed on top of plains. The basin rim is prominent near the southern edge from 179°E to 177°W and then (less obviously) heads northward and is obscured by smooth plains and then by March its neighbors and their ejecta. Box indicates the area of Figure 8.

exterior blue plains do indeed include patches of redder material. Because the color edges are diffuse, varying the parameters of the classification routine causes the line bounding interior and exterior units to migrate east or west and the patches to grow or shrink or to change in number.

To reconcile the observed spectroscopic [Ernst *et al.*, 2015] and compositional [Weider *et al.*, 2015] differences between exterior and interior plains with the lack of a clear boundary, we suggest that this plains volcanism was fed by multiple vents or fissures spaced apart by a few hundred kilometers. This could have tapped melt sources at different depths and/or involved different degrees of partial melting and/or assimilated crust of different composition during ascent, any of which could explain the gross differences between interior and exterior plains. However, despite the differences between magmas sourced inside and outside the basin, any distinction has been blurred on a local scale by a combination of processes. These include the extent of inward and outward flows of lava and 3 billion years of local redistribution of regolith by impact gardening [e.g., Arvidson *et al.*, 1975].

### 3.1.2. Location 6

In the east-southeast of the basin, there is a 100 km wide missing or flooded part of the rim extending from the southern end of an area of semicontinuous blocks of rim material at 176.7°W, 26.8°N (mantled by ejecta from an 80 km Mansurian age crater named March) to 176.7°W, 24.4°N (Figures 7 and 8). This area is exceedingly well covered by high-resolution images, as good as about 37 mpp. Notwithstanding the complexity caused by 2–5 km wide chains of overlapping secondary craters (catenae) that radiate southward from March and a cluster of putative volcanic vents surrounded by “red spots,” the effusive volcanology of this area is clear. As in location 4, smooth plains marked by wrinkle ridges extend from the basin interior eastward through the breach in the rim into exterior plains that are similar in all but color and XRS (X-Ray Spectrometer) composition [Ernst *et al.*, 2015; Weider *et al.*, 2015].

With slight differences in marking the geological contacts, Goosmann *et al.* [2016] and Guzzetta *et al.* [2017] show the exterior plains here as smooth plains passing outward into Odin Formation after about 100 km. At

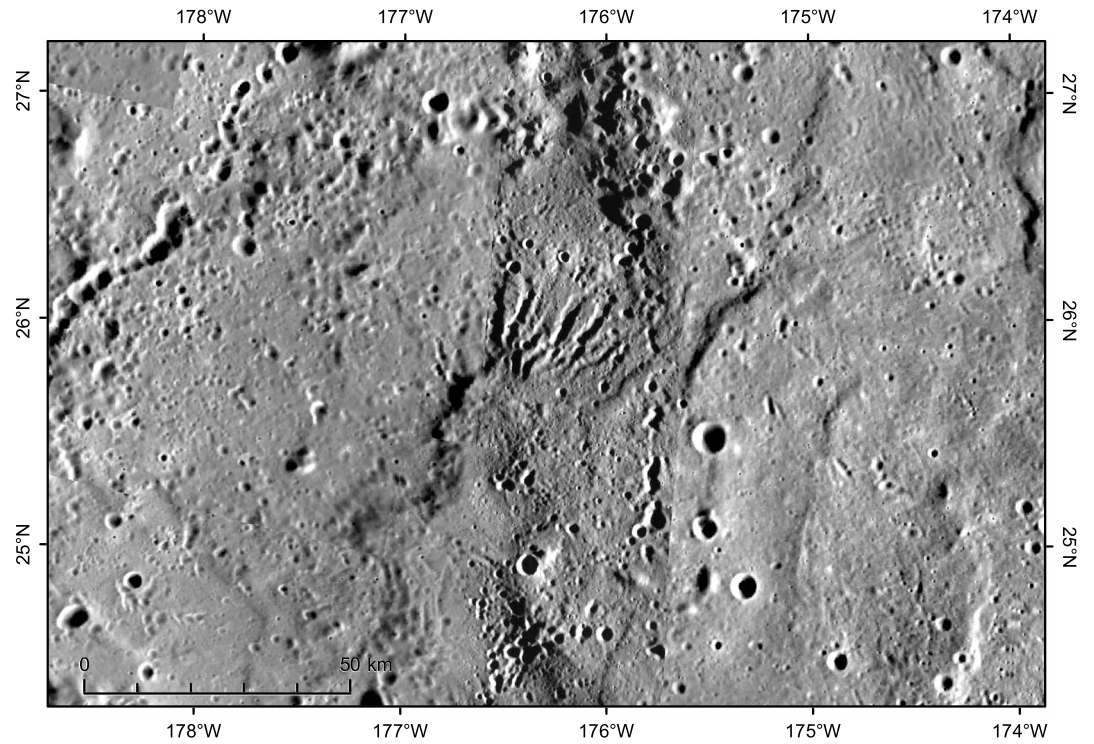


**Figure 8.** The crucial part of location 6. Interior plains to the left and exterior plains to the right. Note the slightly fan-shaped array of 20 km long fractures near the center. This is a mosaic in which every image is better resolution than the 166 mpp base map.

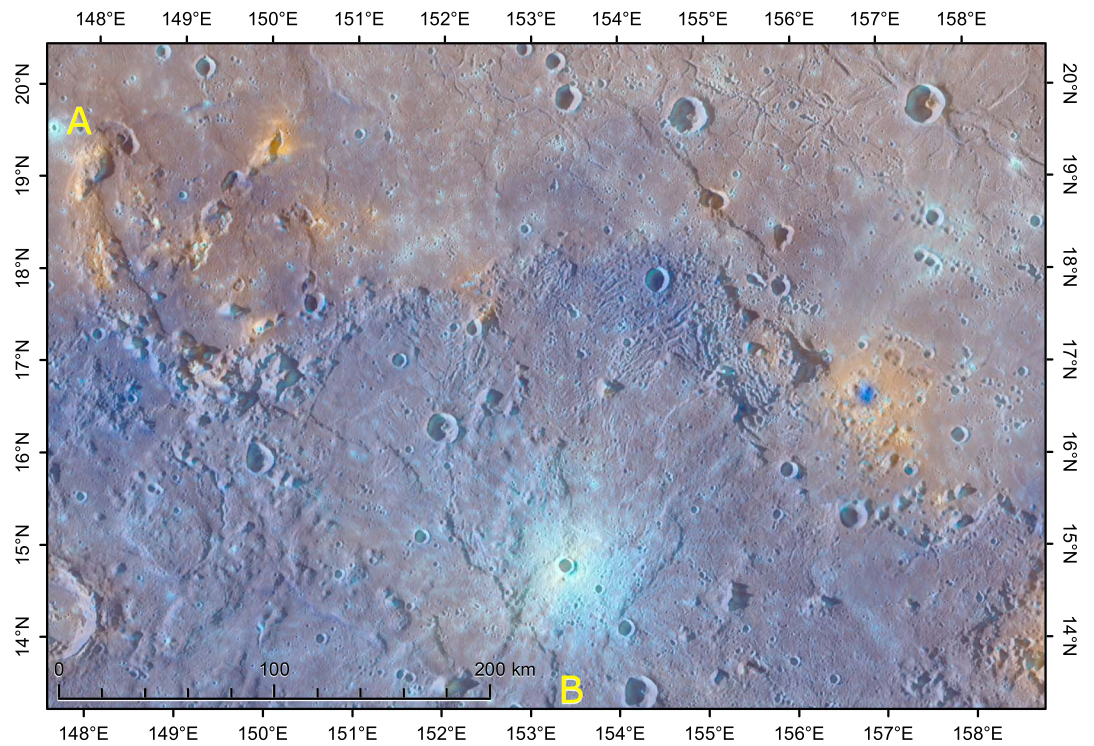


**Figure 9.** Location 1, with 665 mpp WAC color overlay on 166 mpp NAC mosaic. The color change between redder interior plains and bluer exterior plains is not sharp and takes effect over several tens of kilometers, even when the brighter red spots that are regarded as younger pyroclastic deposits are discounted. A lobate scarp (A-B) enters the southern edge of the frame near 153°E and extends almost all the way to the northern edge near 148°E.

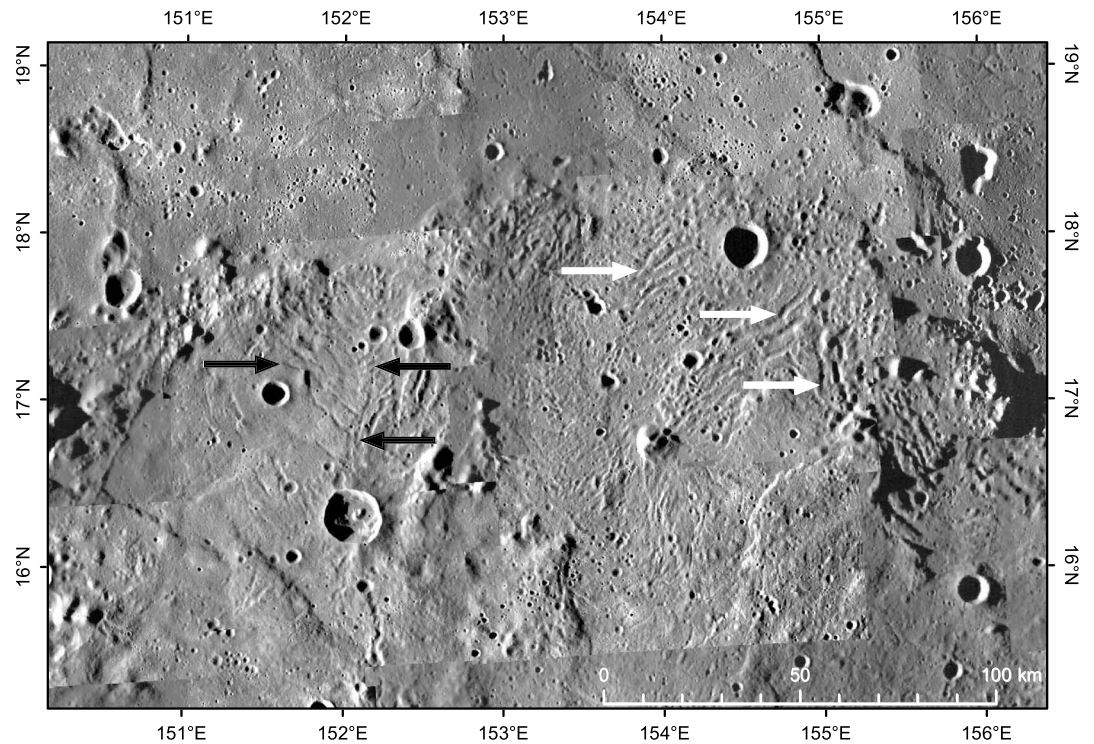


**Figure 10.** Detail of location 1, in the north center of Figure 9. High-resolution frames are superimposed on the 166 mpp NAC mosaic. At this scale, there is little extra insight to be gained about the surface textural features that seem to have been inherited from the flow emplacement. Several clusters and streaks of kilometer-sized secondary impact craters are apparent. Black arrows indicate possible distributary channels. White arrows show structures more similar to the fractures at location 6 in Figure 8.

176.5°W, 26°N, approximately where the buried rim (or a gap if it was originally discontinuous) must lie, there is a slightly fan-shaped array of about eight 3 km wide, steep-sided, flat-bottomed fractures (Figure 8) reminiscent of those occurring more abundantly in locations 1 and 3. We have been able to obtain one depth measurement thanks to a fortuitously placed track by MESSENGER's Mercury Laser Altimeter (MLA) [Cavanaugh *et al.*, 2007] that suggests a depth of 200–300 m.

These could be channels (which would require flow parallel to the rim), but our preferred explanation is that they are stretch marks in the lava crust over a step in the preflow topography. A possible analogy is to the fractured (rough) member of the Maunder Formation of the Moon's Orientale basin. The preferred explanation for that [Head, 1974; Spudis *et al.*, 2014] is a melt sheet cooling and settling over a rugged substrate, but the same effect could result from a thick lava flow in the same situation. The latter is more likely here because of the weight of evidence in favor of this being postbasin, plains-forming lava.

It is not apparent whether any step at the time of emplacement was downward into or out of the basin, and hence, there is no strong evidence as to whether lava flow was inward to or outward from the basin. There is no discernible flow front in this area, and any mapped boundary between interior and exterior plains has to be arbitrary, in the same manner as location 4.

### 3.2. Plains Unit Flow Dominantly Into the Caloris Basin

We present two examples: locations 1 and 3 (see Figure 1 for location).

#### 3.2.1. Location 1

Location 1 gives the impression of a lava delta (Figures 9 and 10). Although there are some features that could be interpreted as distributary channels, the morphology is complicated by later contractional tectonic features that could be mapped as either lobate scarps or wrinkle ridges. The largest of these, more symmetrical in profile than the westerly illumination implies, trends north-south in the south of Figure 9 and bends toward a more northwesterly direction as it is traced northward. It passes onto undoubted interior plains in the

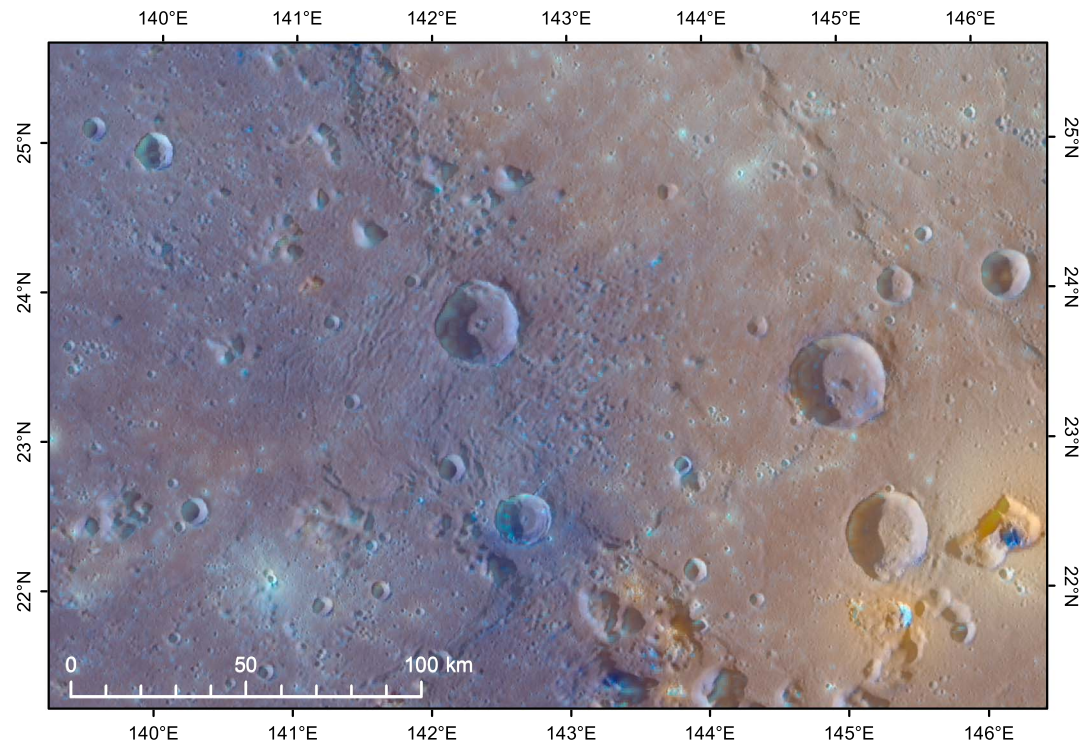


**Figure 11.** Location 3, with 665 mpp WAC color overlain on 166 mpp NAC mosaic.

northwest of Figure 9, making it a rare example of a tectonic feature that crosses the edge of a basin. It is of similar scale to its nearest neighbor, which is an identically verging lobate scarp, named Alvin Rupes but apparently unstudied, which lies just beyond the southern edge of the figure.

Of more relevance to possible emplacement mechanisms is the finer-scale fractured texture in the distal parts of the “delta,” which we have examined on high-resolution (~30 mpp) images. MLA provides no usable depth measurements for any of these fractures, which appear to be similar in scale to the (less complexly patterned) fractures in location 6. The fractured texture is reminiscent of distributary channels north of a 15 km superposed crater at 152°E (black arrows in Figure 10). Other texture (white arrows in Figure 10) can plausibly be interpreted as large-scale rafts of lava crust that was stretched or otherwise disrupted by flow over the basin-bounding scarp (similar to the Maunder Formation analogy that we draw for location 6 or large-scale versions of terrestrial examples such as in *Guest and Stofan* [2005] and *Cashman et al.* [2006]) or alternatively as ogives or “flow ridges” [e.g., *de Silva et al.*, 1994] although the latter would probably require higher flow viscosity than is likely on Mercury [*Sehlke and Whittington*, 2015].

The color boundary between redder interior plains and bluer exterior plains forming the delta is diffuse on a scale of tens of kilometers rather than “sharp” as claimed by *Denevi et al.* [2013], but the place to draw the southern limit of the interior plains on any map is clearly at the foot of the scarp. The delta is consistent with construction by northward flow of exterior plains into the basin, but we cannot rule out interior plains subsequently flooding southward to embay the delta front. *Goosmann et al.* [2016] map the most proximal 500 km of the plains extending south of here as “Odin Formation,” apparently purely based on the presence of embayed knobs (which does not prohibit an origin a lava flows), before changing distally to smooth plains.

### 3.2.2. Location 3

Here as for location 2, the exterior plains have most plausibly flowed toward the basin from a region of exterior plains that is less blue, more red than the source area for location 1 but still less red than the interior plains (Figure 11). This part of the Caloris rim was noted by *Denevi et al.* [2013] as containing “evidence for channelized flow from the Odin-type plains into the basin.” Studied now at higher resolution (as good as 110 mpp), we find no narrow channels but a 50 km wide largely flooded rim reentrant (extending over 80 km outward from the basin) into which exterior/Odin plains material appears to have spilled, carrying knobs up to 3 km in size for a distance of up to 50 km into the basin. The surface in the reentrant itself is marked by “stretch marks”

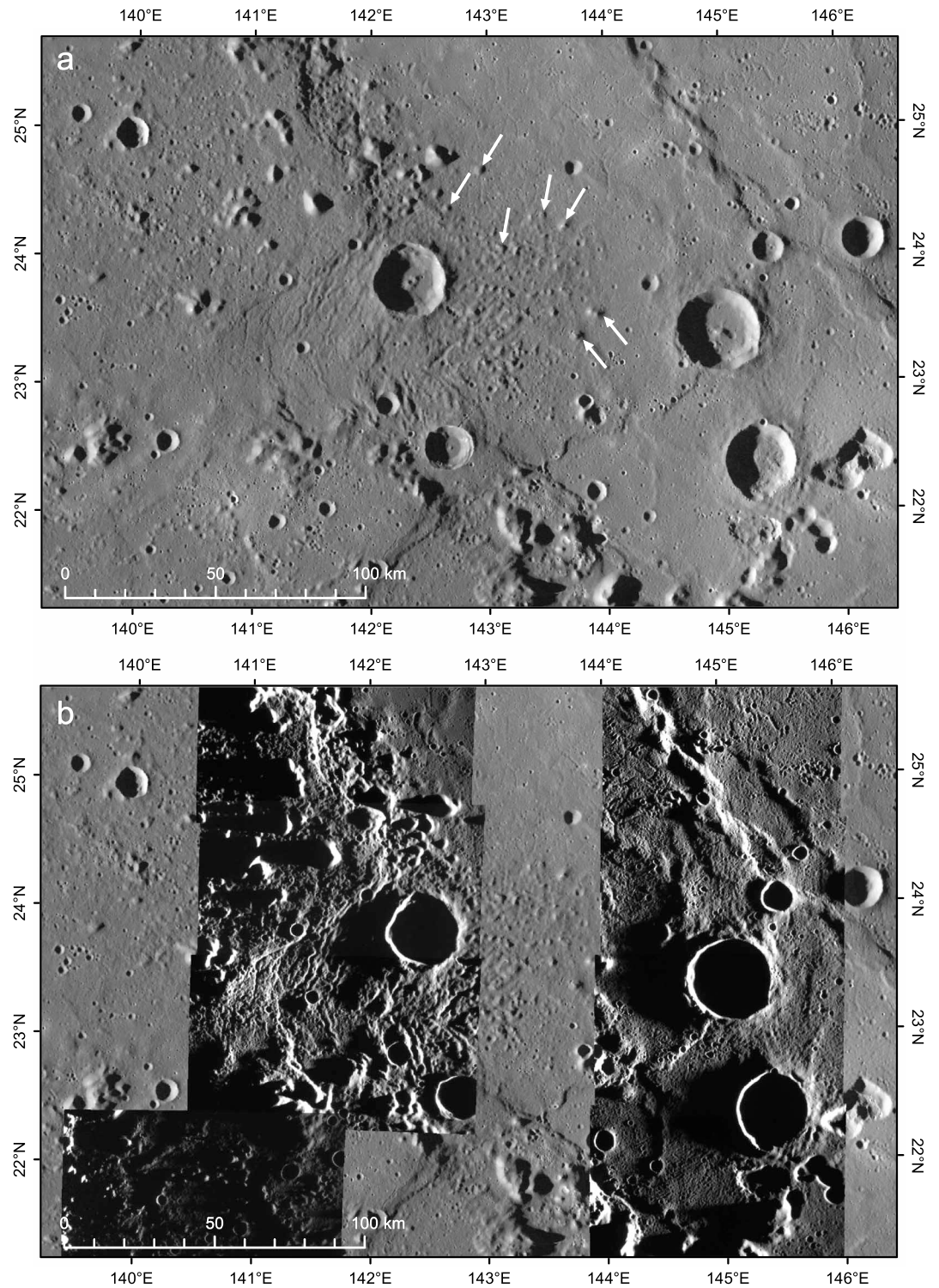


**Figure 12.** Location 3 (a) 166 mpp NAC mosaic. Arrows indicate some of the larger of the more distal knobs of blue material transported into the basin. (b) The same area incorporating nine 110 mpp very high Sun angle (grazing incidence) frames.

in the form of grabens or steps at 2–6 km spacing (Figures 12a and 12b), with a depth that we were able to measure on a single MLA profile as 80–100 m. Our interpretation is that the flow material making the descent into the basin (less than 0.5 km vertically here) had a crust that was torn open but not totally disrupted in the process, unless to form the knobs that are apparent at the distal end.

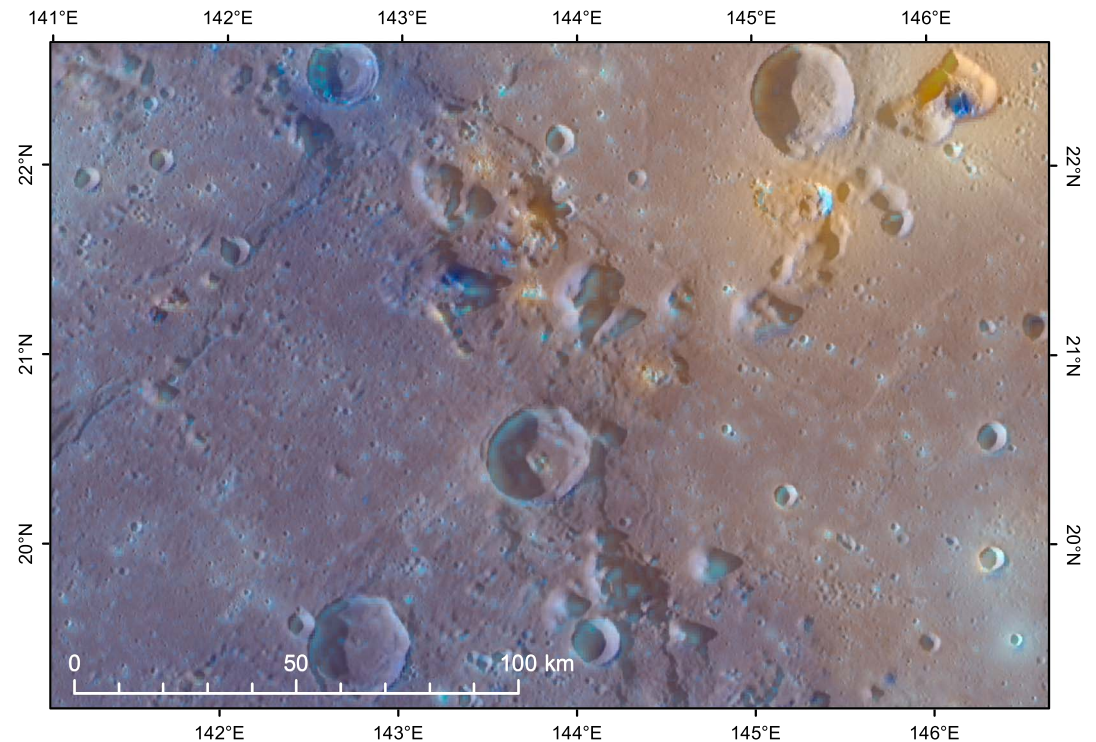


**Figure 13.** Location 2, with 665 mpp WAC color overlay on 166 mpp NAC mosaic. The volcanic vent near the upper right is discussed at length in *Rothery et al.* [2014]. The area shown overlaps in the north with Figure 11.

The most parsimonious explanation for what we observe is a single phenomenon: flow of lava (not impact melt, for reasons elaborated in section 1) across characteristic rim architecture. This is consistent with features in common with locations 1 and 3. For this reason we favor it over alternatives such as the knobs on the basin floor having been emplaced by a landslide (noting that we do not find similar fields of knobs on the interior plains near the openings of reentrants that lack associated signs of inward flooding) or the “grabens” on the flow surface being tectonic in origin. We find no evidence of flow fronts, but the most distal knobs are within plains material that is red rather than blue, so the final flow event here was most likely outward from the basin to embay an already-emplaced inward flow.

### 3.3. Evidence for Plains Unit Flow Outward From the Caloris Basin

We present two examples: locations 2 and 5 (see Figure 1 for location).

#### 3.3.1. Location 2

Progressing clockwise from location 1 as far as, and including, location 2, radial architecture extends for up to 400 km beyond the basin rim, but it is draped by plains material containing numerous isolated knobs. This is usually mapped as Odin Formation [e.g., *Fassett et al.*, 2009; *Goosmann et al.*, 2016] although it transitions gradually outward into uncontested exterior plains so that any mapped boundary between the two is somewhat arbitrary.

We focus here on the ground immediately north and south of a superposed 22 km impact crater centered at 143.8°E, 20.5°N, where the appearance on the 166 mpp mosaic is of plains material that originated beyond the Caloris rim flowing eastward and cascading down to the basin floor (Figures 13 and 14, especially on the north and south sides of the 20 km crater at 144°E). However, there is also evidence, described below, that the latest episode of flow at the edge of the basin was outward.

The most useful additional insight comes from a set of four overlapping ~110 mpp images recorded at very high Sun angle, when the Sun was very low in the east (Figure 14b). These neither add to nor detract from the case for exterior/Odin plains material having cascaded into the basin, but they do accentuate a possible west facing flow front (i.e., the front of a flow emplaced in a westerly direction) at the edge of the interior plains unit. This can be made out also on the lower Sun angle 166 mpp NAC mosaic (Figure 14a) on which it is

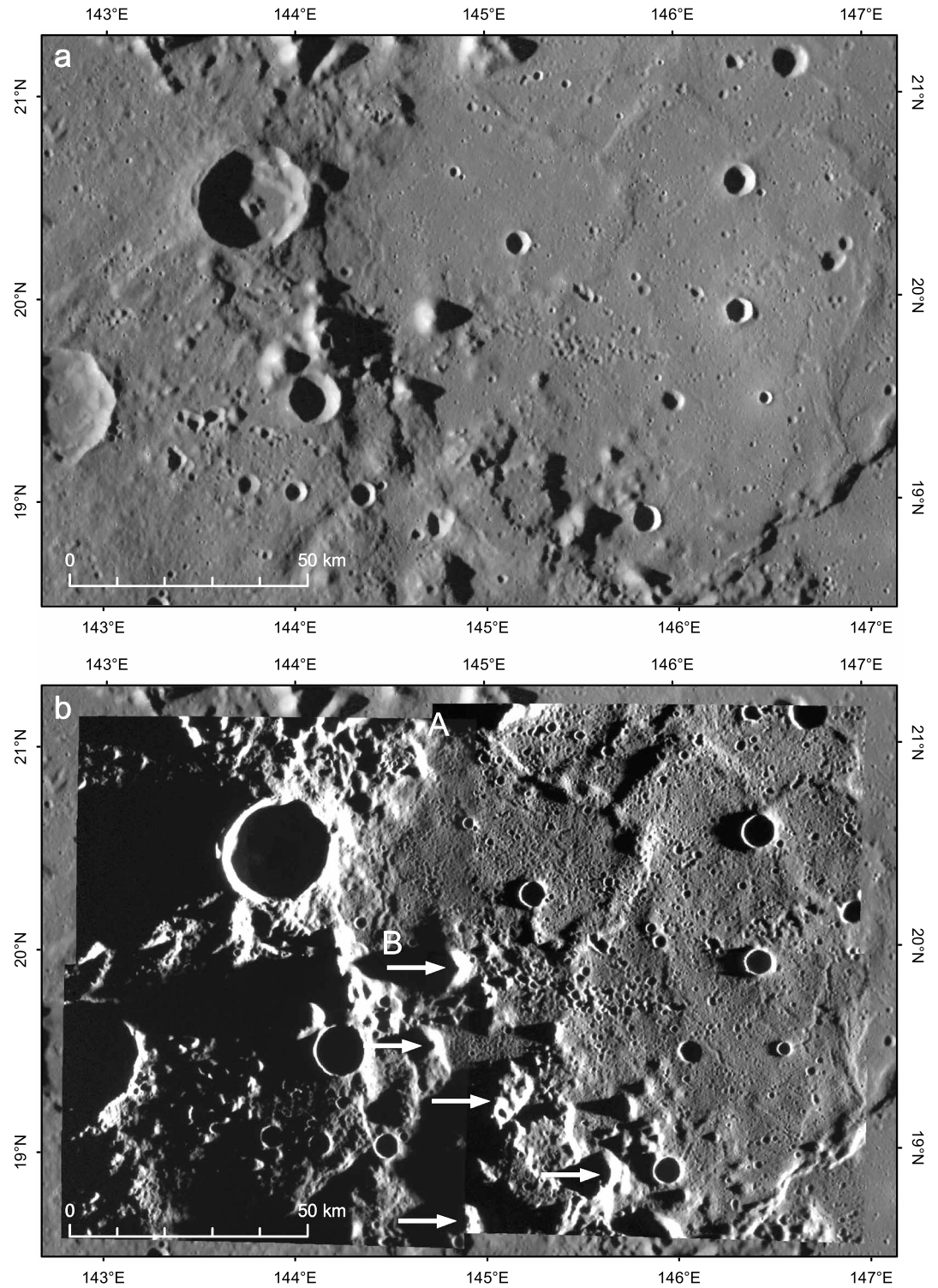


**Figure 14.** Detail of location 2. (a) 166 mpp NAC mosaic. The Caloris rim scarp is embayed by interior plains in the southern half, but both north and south of a 22 km superposed crater near 143.8°E, 20.5°N exterior plains material appears to have cascaded eastward down to the basin floor. (b) Four ~110 mpp very high Sun angle frames. The west facing scarp A-B may be a flow front at the edge of the interior plains. Arrows indicate examples of embayed blocks of rim material.

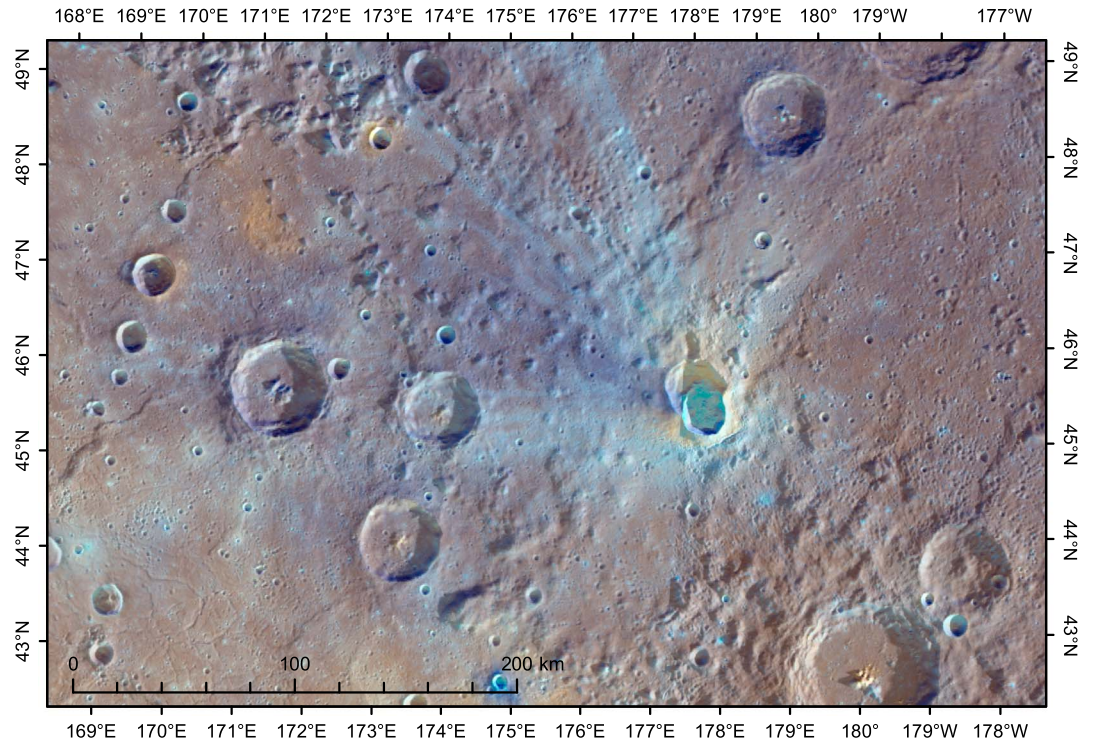


**Figure 15.** Location 5, with 665 mpp WAC color overlain on 166 mpp NAC mosaic. The rayed crater at 178°E is Ailey.

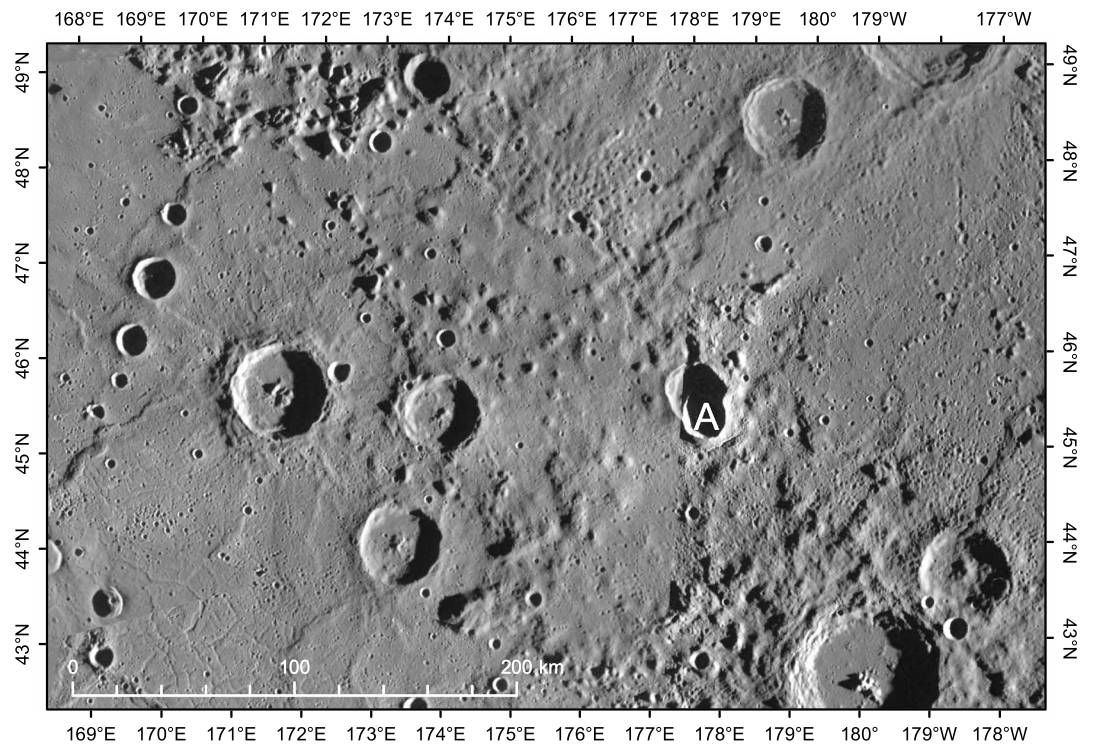


**Figure 16.** Location 5 166 mpp NAC mosaic. The basin rim runs from the upper left to the lower edge at about 177°E. Note the possible outward facing flow front that can be traced northwestward beyond the rim of Ailey (point A), which is 100 km beyond the Caloris rim.

apparent that the surface albedo is slightly higher to the east than to the west. An alternative explanation that the scarp is a tectonic feature is less plausible, because although thrusts on Mercury often approach the surface near the edges of basin-confined flow units, this feature is more sinuous on a small scale than we typically see for those tectonic features [Fegan *et al.*, 2017].

If correct, this is evidence that the interior plains here are locally the younger of the two. The interior plains clearly embay sub-10 km scale blocks of rim material. The high Sun angle reveals near saturation of the surface of the interior plains by sub-1 km sized craters, many of which are possibly endogenic given that they appear much less common west of the “flow front,” although we cannot rule out a coincidental cluster of secondaries.

### 3.3.2. Location 5

Our final example is on the northeast rim of the basin. Color interpretation here is complicated by bright rays and one dark ray possibly containing low-reflectance material that emanate from Ailey, a young (Kuiperian age) 25 km crater (Figures 15 and 16). This is another place where the rim is breached by plains material, but the definite gap in the rim (172.0°E, 48.1°N) is only about 20 km wide. Interior plains pass through this and merge imperceptibly into a smooth facies draped over rim material (mapped as Caloris Rough Ejecta by Mancinelli *et al.* [2016] and as Nervo Formation by Goosmann *et al.* [2016]). It is possible that a thick interior flow overtopped the rim here, before deflation caused partial drain back. Farther beyond the rim the terrain is mapped as Odin Formation (clearly superimposed on top of basin-related radial sculpture) and then, more distally, smooth plains. Continuity between interior plains and exterior plains here is plausible but unlikely, and we have been unable to locate any high-resolution images that cast further light on relationships. This area should be a priority target for study by the next Mercury mission, BepiColombo [Rothery *et al.*, 2010].

## 4. Conclusions

Although the interior and exterior plains of the Caloris basin are spectrally and compositionally different, the distinction is not sharp enough to be apparent upon examination of images at high spatial resolution. We have identified evidence at places around the Caloris periphery where there is no clearly definable boundary between interior and exterior plains nor any sign of the direction of flow emplacement (locations 4 and 6). Elsewhere, there is evidence of flow of exterior plains descending the rim scarp and entering the basin (locations 1–3). There are hints of inward flow subsequently embayed by outward flow in locations 2 and 3, whereas location 5 shows clear evidence of outward flow beyond the rim.

The simplest explanation (bearing in mind that crater counting has not been able to separate them) is that emplacement of interior and exterior plains occurred during an overlapping time period and that they were erupted from multiple sources suggesting flow lengths of the order of hundreds but not thousands of kilometers. This is consistent with crater counts, given the errors and limitations of the various methods [Denevi *et al.*, 2009; Fassett *et al.*, 2009; Mancinelli *et al.*, 2016]. The Caloris interior plains have an estimated volume [Ernst *et al.*, 2015] of  $3.2\text{--}5.2 \times 10^6 \text{ km}^3$ , and to this we must add a probably similar volume to account for the exterior plains, suggesting that the order of  $1 \times 10^7 \text{ km}^3$  of lava was emplaced in a single epoch.

Some of our interpretations are necessarily speculative, being limited by the amount and nature of the data. Deeper and firmer understanding must probably await higher-resolution and more complete imagery and compositional mapping by the next mission to Mercury, BepiColombo, from which orbital science data are expected in 2025.

## 5. Data

The enhanced color renderings in Figures 1, 5, 6, 7, 9, 10, 11, 13, and 15 are based on a process that has become standard for MESSENGER color MDIS data [e.g., Denevi *et al.*, 2013; Ernst *et al.*, 2015] in which the data from the 430 nm, 730 nm, and 1000 nm channels are passed through a principal components transformation, after which the second principal component is displayed in red, the first in green, and the 430/1000 nm ratio (i.e., the ratio of blue to near-infrared) is displayed in blue. The results look similar to taking a simple, fairly natural color, three-channel red, green, and blue color composite, and exaggerating the color saturation via an IHS (intensity-hue-saturation) transformation. Basically, colors are stronger (more saturated) but blue still corresponds to original blue and red to original red. This means that comparisons describing units as blue or red are robust and correspond to bluer or redder spectral slopes in the original data.

We used ArcGIS software to process and display Mercury Dual Imaging System (MDIS) monochrome (250 mpp and 166 mpp), color (333 mpp), and enhanced color (665 mpp) global mosaics. We searched the whole Caloris rim to identify places where the rim was breached by smooth plains. We used the MDIS NAC coverage shapefile to find higher-resolution images covering these areas of special interest and imported those into ArcGIS. To minimize distortion, the Mercury images herein are all shown on a Transverse Mercator projection, centered in each case on the midlongitude of each scene center.

We list individual high-resolution frame numbers used in our main figures below, citing representative pixel sizes, in meters per pixel (mpp).

Location 1: High-resolution images used in Figure 10 are EN0220418495M, EN0220418504M, EN0220418514M (27 mpp), EN0220418524M, EN0220418534M, EN0220418544M, EN0220418554M, EN0250681476M, EN0250681492M, EN0250767870M, EN0250767885M, EN0250767900M, EN0250767911M (35 mpp), EN0250767927M, EN0250767943M, EN0250796750M, EN0251027136M, EN0251027149M, and EN0251027162M.

Location 2: High-resolution images used in Figure 14 are EN0243938836M, EN0243938838M, EN0243938874M (111 mpp), and EN0243938876M.

Location 3: High-resolution images used in Figure 12 are EN0243938948M, EN0243938979M, EN0243938913M, EN0243939011M, EN0244025305M, EN0244025341M, EN0244025376M (110 mpp), and EN0244025407M.

Location 4: High-resolution images of the crucial wrinkle ridge at the west of the delta include EN0220720687M (14 mpp), EN0220720692M, EN0251055633M, EN0251055641M, EN1015339115M, and EN1015339129M.

We found no relevant high-resolution images of location 5.

Location 6: Many high-resolution images went into making Figure 8. The most detailed north-south strip at 176°W consists of frames EN0258283508M (37 mpp), EN0258283530M, EN0258283551M, EN0258283571M, and EN0258283591M.

The MLA data that we used to determine the depth of fractures in flow surfaces were MLASCIRDR1108022042 (location 3) and MLASCIRDR1201181443 (location 6). We found no MLA tracks oriented so as to be able to determine heights of the possible flow fronts in locations 2 and 5 or of the wrinkle ridge “A-B” in location 4.

## Acknowledgments

D.A.R. was funded by the UK Space Agency and the Science and Technology Funding Council ST/M002101/1, ST/L000776/1, and ST/N00399X/1. We thank Tracy Gregg and Lionel Wilson for preliminary discussions on some of the images used here and Brett Denevi and anonymous reviewers for helpful comments on earlier versions of the paper. The data used here are available from PDS.

## References

- Arvidson, R., R. J. Drozd, C. M. Hohenberg, C. J. Morgan, and G. Poupeau (1975), Horizontal transport of the regolith, modification of features, and erosion rates on the lunar surface, *The Moon*, *13*, 67–79.
- Becker, K. J., M. S. Robinson, T. L. Becker, L. A. Weller, K. J. Edmondson, G. A. Neumamn, M. E. Perry, and S. C. Solomon (2016), First global digital elevation model of Mercury, *Lunar Planet. Sci. Conf.*, *47*, 2959.
- Byrne, P. K., C. Klimczak, A. M. C. Şengör, S. C. Solomon, T. R. Watters, and S. A. Hauck II (2014), Mercury's global contraction much greater than earlier estimates, *Nat. Geosci.*, *7*, 301–307, doi:10.1038/ngeo2097.
- Byrne, P. K., L. R. Ostrach, C. L. Fassett, C. R. Chapman, B. W. Denevi, A. J. Evans, C. Klimczak, M. E. Banks, J. W. Head, and S. C. Solomon (2016), Widespread effusive volcanism on Mercury likely ended by about 3.6 Ga, *Geophys. Res. Lett.*, *43*, 7408–7416, doi:10.1002/2016GL069412.
- Cashman, K. V., R. C. Kerr, and R. W. Griffiths (2006), A laboratory model of surface crust formation and disruption on lava flows through non-uniform channels, *Bull. Volcanol.*, *68*, 753–770, doi:10.1007/s00445-005-0048-z.
- Cavanaugh, J. F., et al. (2007), The Mercury Laser Altimeter instrument for the MESSENGER mission, in *The Messenger Mission to Mercury*, pp. 451–479, Springer, New York.
- Chabot, N. L., B. W. Denevi, S. L. Murchie, C. D. Hash, C. M. Ernst, D. T. Blewett, H. Nair, N. R. Laslo, and S. C. Solomon (2016), Mapping Mercury: Global imaging strategy and products from the MESSENGER mission, *Lunar Planet. Sci. Conf.*, *47*, 1256.
- de Silva, S. L., P. W. Francis, R. E. Drake, and C. Ramirez (1994), Effusive silicic volcanism in the Central Andes: The Chao dacite and other young lavas of the Altiplano-Puna Volcanic Complex, *J. Geophys. Res.*, *99*, 17,805–17,825, doi:10.1029/94JD00166.
- Denevi, B. W., et al. (2009), The evolution of Mercury's crust: A global perspective from MESSENGER, *Science*, *324*, 613–618, doi:10.1126/science.1172226.
- Denevi, B. W., et al. (2013), The distribution and origin of smooth plains on Mercury, *J. Geophys. Res. Planets*, *118*, 891–907, doi:10.1002/jgre.20075.
- Ernst, C. M., et al. (2015), Stratigraphy of the Caloris basin, Mercury: Implications for volcanic history and basin impact melt, *Icarus*, *250*, 413–429.
- Fassett, C. I., J. W. Head, D. T. Blewett, C. R. Chapman, J. L. Dickson, S. L. Murchie, S. C. Solomon, and T. R. Watters (2009), Caloris impact basin: Exterior geomorphology, stratigraphy, morphometry, radial sculpture, and smooth plains deposits, *Earth Planet. Sci. Lett.*, *285*, 297–308, doi:10.1016/j.epsl.2009.05.022.
- Fegan, E. R., D. A. Rothery, S. Marchi, M. Massironi, S. J. Conway, and M. Anand (2017), Late movement of basin-edge lobate scarps on Mercury, *Icarus*, doi:10.1016/j.icarus.2017.01.005.
- Goosmann, E., D. L. Buczkowski, C. M. Ernst, B. W. Denevi, and M. J. Kinczyk (2016), Geologic map of the Caloris basin, Mercury, *Lunar Planet. Sci. Conf.*, *47*, 1254.

- Goudge, T. A., et al. (2014), Global inventory and characterization of pyroclastic deposits on Mercury: New insights into pyroclastic activity from MESSENGER orbital data, *J. Geophys. Res. Planets*, *119*, 635–658, doi:10.1002/2013JE004480.
- Guest, J. E., and E. R. Stofan (2005), The significance of slab-crust lava flows for understanding controls on flow emplacement at Mount Etna, Sicily, *J. Volc. Geother. Res.*, *142*, 193–205.
- Guzzetta, L., V. Galluzzi, L. Ferranti, and P. Palumbo (2017), Geology of the Shakespeare Quadrangle, Mercury (H03), *J. Maps*, doi:10.1080/17445647.2017.1290556.
- Hawkins, S. E., III, et al. (2007), The Mercury Dual Imaging System on the MESSENGER spacecraft, *Space Sci. Rev.*, *131*, 247–338, doi:10.1007/s11214-007-9266-3.
- Head, J. W. (1974), Orientale multi-ringed basin interior and implications for the petrogenesis of lunar highland samples, *The Moon*, *11*, 327–356.
- Head, J. W., et al. (2009), Volcanism on Mercury: Evidence from the first MESSENGER flyby for extrusive and explosive activity and the volcanic origin of plains, *Earth Planet. Sci. Lett.*, *285*, 227–242, doi:10.1016/j.epsl.2009.03.007.
- Head, J. W., et al. (2011), Flood volcanism in the northern high latitudes of Mercury revealed by MESSENGER, *Science*, *333*, 1853–1856, doi:10.1126/science.1211997.
- Holsapple, K. A., and K. R. Housen (2007), A crater and its ejecta: An interpretation of Deep Impact, *Icarus*, *187*, 345–356.
- Izenberg, N. R., et al. (2014), The low-iron, reduced surface of Mercury as seen in spectral reflectance by MESSENGER, *Icarus*, *228*, 364–374.
- James, B. B., M. T. Zuber, R. J. Phillips, and S. C. Solomon (2015), Support of long-wavelength topography on Mercury inferred from MESSENGER measurements of gravity and topography, *J. Geophys. Res. Planets*, *120*, 287–310, doi:10.1002/2014JE004713.
- Kerber, L. A., J. W. Head, S. C. Solomon, S. L. Murchie, D. T. Blewett, and L. Wilson (2009), Explosive volcanic eruptions on Mercury: Eruption conditions, magma volatile content, and implications for interior volatile abundances, *Earth Planet. Sci. Lett.*, *285*, 263–271, doi:10.1016/j.epsl.2009.04.037.
- Kerber, L. A., J. W. Head, D. T. Blewett, S. C. Solomon, L. Wilson, S. L. Murchie, M. S. Robinson, B. W. Denevi, and D. L. Domingue (2011), The global distribution of pyroclastic deposits on Mercury: The view from MESSENGER flybys 1–3, *Planet. Space Sci.*, *59*, 1895–1909.
- Mancinelli, P., F. Minelli, C. Pauselli, and C. Federico (2016), Geology of the Raditladi Quadrangle, Mercury (H04), *J. Maps*, doi:10.1080/17445647.2016.1191384.
- McCaughey, J. F., J. E. Guest, G. R. Schaber, N. J. Trask, and R. Greeley (1981), Stratigraphy of the Caloris basin, Mercury, *Icarus*, *47*, 184–202.
- McNutt, R. L., et al. (2014), MESSENGER at Mercury: Early orbital operations, *Acta Astronaut.*, *93*, 509–515.
- Murchie, S. L., et al. (2008), Geology of the Caloris basin, Mercury: A view from MESSENGER, *Science*, *321*, 73–76.
- Murchie, S. L., et al. (2015), Orbital multispectral mapping of Mercury with the MESSENGER Mercury Dual Imaging System: Evidence for the origins of plains units and low-reflectance material, *Icarus*, *254*, 287–305.
- Murray, B. C., R. G. Strom, N. J. Trask, and D. E. Gault (1975), Surface history of Mercury: Implications for terrestrial planets, *J. Geophys. Res.*, *80*, 2508–2514, doi:10.1029/JB080i017p02508.
- Oberst, J., F. Preusker, R. J. Phillips, T. R. Watters, J. W. Head, M. T. Zuber, and S. C. Solomon (2010), The morphology of Mercury's Caloris basin as seen in MESSENGER stereo topographic models, *Icarus*, *209*, 230–238.
- Robinson, M. S., et al. (2008), Reflectance and color variations on Mercury: Regolith processes and compositional heterogeneity, *Science*, *321*, 66–69.
- Rothery, D. A. (2015), *Planet Mercury: From Pale Pink Dot to Dynamic World*, Springer-Praxis, Heidelberg, doi:10.1007/978-3-319-12117-8.
- Rothery, D. A., et al. (2010), Mercury's surface and composition to be studied by BepiColombo, *Planet. Space Sci.*, *58*, 21–39.
- Rothery, D. A., R. T. Thomas, and L. Kerber (2014), Prolonged eruptive history of a compound volcano on Mercury: Volcanic and tectonic implications, *Earth Planet. Sci. Lett.*, *385*, 59–61.
- Sehlke, A., and A. G. Whittington (2015), Rheology of lava flows on Mercury: An analog experimental study, *J. Geophys. Res. Planets*, *120*, 1924–1955, doi:10.1002/2015JE004792.
- Spudis, P. D., D. J. P. Martin, and G. Kramer (2014), Geology and composition of the Orientale basin impact sheet, *J. Geophys. Res. Planets*, *119*, 19–29, doi:10.1002/2013JE004521.
- Strom, R. G., C. R. Chapman, W. J. Merline, S. C. Solomon, and J. W. Head (2008), Mercury cratering record viewed from MESSENGER's first flyby, *Science*, *321*, 79–81, doi:10.1126/science.1159317.
- Thomas, R. J., D. A. Rothery, S. J. Conway, and M. Anand (2014), Long-lived explosive volcanism on Mercury, *Geophys. Res. Lett.*, *41*, 6084–6092, doi:10.1002/2014GL061224.
- Weider, S. Z., et al. (2015), Evidence for geochemical terranes on Mercury: Global mapping of major elements with MESSENGER's X-ray spectrometer, *Earth Planet. Sci. Lett.*, *416*, 109–120.
- Zuber, M. T., et al. (2012), Topography of the Northern Hemisphere of Mercury from MESSENGER Laser Altimetry, *Science*, *336*, 217–220.